Nereid from space: Rotation, size and shape analysis from Kepler/K2, Herschel and Spitzer observations

Cs. Kiss,[1] A. Pál,[1,2] A. I. Farkas-Takács[1,2] Gy. M. Szabó,[1,3,4] R. Szabó,[1]
L. L. Kiss,[1,4,5] L. Molnár,[1] K. Sárneczky,[1,4] Th.G. Müller,[6] M. Mommert,[7]
and J. Stansberry[8]

[1] *Konkoly Observatory, Research Centre for Astronomy and Earth Sciences, Hungarian Academy of Sciences*
H-1121 Budapest, Konkoly Thege Miklós út 15-17, Hungary
[2] *Eötvös Loránd Tudományegyetem, H-1117 Pázmány Péter sétány 1/A, Budapest, Hungary*
[3] *ELTE Gothard Astrophysical Observatory, H-9704 Szombathely, Szent Imre herceg út 112, Hungary*
[4] *Gothard-Lendület Research Group, H-9704 Szombathely, Szent Imre herceg út 112, Hungary*
[5] *Sydney Institute for Astronomy, School of Physics A28, University of Sydney, NSW 2006, Australia*
[6] *Max-Planck-Institut für extraterrestrische Physik, Postfach 1312, Giessenbachstr., 85741 Garching, Germany*
[7] *Department of Physics and Astronomy, Northern Arizona University, P.O. Box 6010, Flagstaff, AZ 86011, USA*
[8] *Space Telescope Science Institute, 3700 San Martin Dr., Baltimore, MD 21218, United States*

12 January 2016

ABSTRACT

In this paper we present an analysis of Kepler K2 mission Campaign 3 observations of the irregular Neptune satellite, Nereid. We determined a rotation period of $P = 11.594 \pm 0.017$ h and amplitude of $\Delta m = 0^{\mathrm{m}}0328 \pm 0^{\mathrm{m}}0018$, confirming previous short rotation periods obtained in ground based observations. The similarities of light curve amplitudes between 2001 and 2015 show that Nereid is in a low-amplitude rotation state nowadays and it could have been in a high-amplitude rotation state in the mid 1960's. Another high-amplitude period is expected in about 30 years. Based on the light curve amplitudes observed in the last 15 years we could constrain the shape of Nereid and obtained a maximum a:c axis ratio of 1.3:1. This excludes the previously suggested very elongated shape of a:$c \approx$ 1.9:1 and clearly shows that Nereid's spin axis cannot be in forced precession due to tidal forces. Thermal emission data from the Spitzer Space Telescope and the Herschel Space Observatory indicate that Nereid's shape is actually close to the a:c axis ratio limit of 1.3:1 we obtained, and it has a very rough, highly cratered surface.

Key words: methods: observational — techniques: photometric — astrometry — planets and satellites: individual: Neptune II Nereid

1 INTRODUCTION

Nereid is a large, ~350 km sized, irregular satellite orbiting Neptune in a very eccentric and inclined orbit (Dobrovolskis 1995; Jacobson 2009). Although its orbital characteristics are well known, there is still a mistery related to its shape, orientation and rotation rate. There have been several papers reporting on unusual, in some cases large amplitude brightness variations of Nereid on different timescales, from night-to-night variations to changes on annual scales. These investigations are nicely summarised and discussed in Schaefer et al. (2008). In this paper the authors' preferred solution that could explain the photometric variability was that year-to-year variations are caused by Nereid's pole precessing, in some years Nereid's pole pointing towards Earth

while in other years nearly perpendicular to the line of sight. Physically this could be explained by forced precession, due to Neptune's tidal torque on a non-spherical Nereid. This would require high, 1.9:1 or greater axis ratios.

Hesselbrock et al. (2013) attempted to model the rotation of Nereid in a way similar to Schaefer et al. (2008), but also considering the effect of smaller bodies in addition to the Sun and Neptune, especially that of Triton. Their "best estimate" solution is a triaxial ellipsoid with semiaxis ratios of c/a~0.5, b/a~0.6, an inital obliquity of ~60° and an initial rotation period of 144 h. Their model predicts "active" and "inactive" periods, depending on the actual direction of the main spin axis (c-axis aspect angles of ~90° and ~0°, respectively), matching the photometry data collected in Schaefer et al. (2008) qualitatively, however, with some differences in

the predicted brightness levels compared with the observed ones. They explain this latter discrepancy by an additional effect of a non-uniform albedo distribution. Their model predicts a ∼15-year time between the two extreme orientations.

While the shape of Nereid would be essential for the rotation evolution models, this is not known. Thomas et al. (1991) derived a size of 350±50 km from Voyager-2 flyby observations in which Nereid was resolved to some level, but the quality of the data was not good enough to constrain the shape (see also Schaefer et al. 2008, for a discussion).

Based on observations in August 2001 and August 2002 Grav, Holman & Kavelaars (2003) derived a short rotation period of $P = 11^{\rm h}52$ for Nereid with a small peak-to-peak light curve amplitude of $0^{\rm m}029 \pm 0.003$. This rotation period was later questionned by Schaefer et al. (2008) due to the relatively poor sampling of the rotation curve, and has not been included in the analysis by Hesselbrock et al. (2013) either. Terai & Itoh (2013) obtained a very similar light curve ($\Delta m = 0^{\rm m}031 \pm 0^{\rm m}001$, $P = 11^{\rm h}50 \pm 0^{\rm h}10$) based on observations in 2008, but their light curve was sparsely sampled in terms of rotational phase.

As shown above, ground based observations have not placed a strong constraint on the rotation of Nereid. However, as it has been demonstrated in some recent papers (Pál et al. 2015a,b), data from the extended Kepler mission (K2, Howell et al. 2014) can be very effectively used to obtain rotational light curves of distant Solar System bodies due to uninterrupted photometric time series of several tens of days in length. Given that Neptune, and therefore Nereid as well, was included in the Campaign 3 observations of the K2 mission, we attempted to obtain the light curve of Nereid from these observations. In addition to the light curve data, we collected archival Spitzer Space Telescope and Herschel Space Observatory data to detect the thermal emission of Nereid in the mid- and far-infrared (24–160 μm) wavelength ranges. In this paper, with the synergy of the light curve information and thermal emission data, we put important constraints on the rotational state, shape, as well as on other physical properties of Nereid.

2 THE KEPLER K2 LIGHT CURVE

2.1 K2 observations

Kepler observed Nereid during the third campaign of the extended mission, named K2 (Howell et al. 2014). In this K2 mission, *Kepler* targets fields near the Ecliptic, observing each field for approximately three months. This quarterly schedule allows the continuous observations of Solar System bodies if sufficiently large arcs are allocated in the CCD mosaic of the *Kepler* space telescope. Main-belt asteroids have a large apparent motion (comparable to or even larger than the total field-of-view of the space telescope). In addition, main-belt asteroids have a non-negligible noise source on the photometry of stellar targets (Szabó et al. 2015). However, minor bodies outside the main-belt – such as Centaurs and trans-Neptunian objects – can be observed with a relatively low pixel budget. In addition, the pixel budget can even be minimized around the stationary point, where masks with a size of ∼ 20 × 20 pixels can be sufficient to follow trans-Neptunian objects up to 10 − 15 days (Pál et al. 2015a).
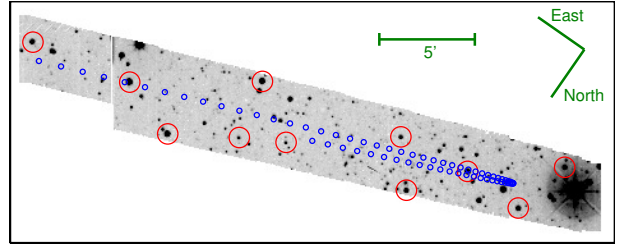

Figure 1. The field-of-view of *Kepler*, showing the field in which Neptune and Nereid was apparently moving during the K2 Campaign 3. The stars involved in the determination of the absolute and differential astrometric solutions are indicated by red circles. The small blue circles indicate the position of Nereid with a 1-day stepsize throughout the observations. The total size of the field is 475×190 pixels, i.e. ∼ $32' \times 13'$. This image is shown in the CCD frame, hence the image is flipped with respect to the standard view.

In the case of Nereid, a nearly parallelogram-shaped field was allocated for *Kepler*/K2 observations. This field includes the apparent track of both Neptune and Nereid and has a size of 456×80 pixels. This field is located on *Kepler* module #13 and read out by its output amplifier #2 (i.e. channel #42 considering the full mosaic array). In order to analyze the field, we retrieved the 456 individual data frames corresponding to the columns of this parallelogram-shaped CCD area. Thereafter, we built the individual image frames on a rectangular area having a size of 475×190. This area safely covers the parallelogram and includes some additional rows and columns in order to have same extra space for frame registration. In total, the corresponding data series contains 3336 individual and useable long-cadence frames. The total number of frames for Campaign 3 were 3386, but 50 frames had to be dropped due to lack of data or inappropriate tracking during the exposure.

Due to the lack of a third active reaction wheel, the positioning jitter of *Kepler*/K2 is significantly larger than what it had been during the main mission. Therefore, the 3336 frames have to be analyzed independently in order to retrieve the proper astrometric solution as well as to perform an image registration needed by the subsequent steps of differential photometry. To accomplish this astrometry, we selected nearly a dozen reference stars distributed uniformly in the field. Due to the large size of the field, we did not include additional stamps for this purpose (see e.g. the case of 2007 OR$_{10}$, Pál et al. 2015b). These stars were used to perform both the differential astrometry (i.e. the frame registration) and the absolute astrometry (i.e. finding the plate solution w.r.t. the J2000 system). The absolute plate solution has been derived by cross-matching the pixel coordinates of the selected reference stars with the USNO-B catalogue (Monet et al. 2003). These 11 stars were also used to transform *Kepler*/K2 photometry to USNO-B1 R system. The USNO magnitudes of these star cover the range of $R = 13.2 \ldots 17.8$, nearly homogeneously. Since an unfiltered CCD efficiency curve can be considered as a "wide R" band, the comparison of the USNO magnitudes with the instrumental ones yielded a fit residual of 0.12 magnitudes. Therefore, we can state that the accuracy of this transformation is in this range.

In all other aspects, the data reduction and photome-

try were conducted in a similar manner as it was described in Pál et al. (2015a) or Pál et al. (2015b). Our photometric pipeline used for *Kepler* frame reconstruction, source extraction, astrometry and cross-matching, image registration and differential photometry are based on the various tasks of the FITSH package (Pál 2012). The folded light curve (with the period of 11.594 h, see Sect. 2.2) of Nereid is shown in Fig. 2. We note here that the formal photometric uncertainities on the individual frames increased from 0.012 up to 0.022 throughout this ∼ 67 days long campaign. This increment is due to the gradually increasing level of zodiacal light as the elongation of Nereid decreased from 140° down to 74°. This instrumental uncertainty can be compared with the statistical one computed from the root mean square deviation of the photometric data points on each of the $N = 20$ bins on the binned light curve. This latter method gives us an estimation of $0.028 - 0.034$ error for each frame, i.e. slightly larger than the instrumental estimate.

2.2   Light curve analysis

Based on previous studies in the literature, the expected amplitude of the light curve variations are relatively small. Therefore, periodicity in the light curve has been searched by assuming a sinusoidal function coadded to a linear function representing the gradual fading of the object (due to phase angle and distance variations). This function was defined as

$$A + B\Delta t + C\cos(2\pi n\Delta t) + D\sin(2\pi n\Delta t), \qquad (1)$$

where n is the suspected rotational frequency and Δt is the time after $2,457,010$ JD (chosen in order to minimize the rounding errors and numerical artifacts). The unknown parameters A, B, C and D can then be derived using linear regression. The parameter space in n is then scanned in the physically relevant domain with a stepsize comparable to one tenth of the reciprocal timespan of the observations (i.e. $0.001\,\mathrm{d}^{-1}$). A prominent peak has been detected in the fit residuals at $n = 4.140 \pm 0.006$ c/d, as it can also be well seen in Fig. 2b. The corresponding values for the four coefficients at this peak was found to be $\mathbf{A} = 19.3650 \pm 0.0006$, $B = 0.00335 \pm 0.00003$, $C = 0.0129 \pm 0.0008$ and $D = 0.0101 \pm 0.0008$. The hypotenuse of C and D, i.e. $\sqrt{C^2 + D^2}$ gives us an estimation for the total amplitude which is then 0.0164 ± 0.0008. The residual of the fit was found to be 0.031 magnitudes. Due to the significance of this peak, we conclude that the rotation period is either $P = 5.797 \pm 0.008\,\mathrm{h}$ or its double, $P = 11.594 \pm 0.017\,\mathrm{h}$, assuming a double-peaked solution. The amplitude of the light curve is $0\overset{\mathrm{m}}{.}0164 \pm 0\overset{\mathrm{m}}{.}0008$ ($0\overset{\mathrm{m}}{.}0328 \pm 0\overset{\mathrm{m}}{.}0018$ peak-to-peak). To correct for phase angle effects, a phase constant of $k = 0.123 \pm 0.005\,\mathrm{mag\,deg}^{-1}$ was also derived from our K2 data (Nereid was seen at phase angles of $1\overset{\circ}{.}2 \le \alpha \le 1\overset{\circ}{.}9$ during the K2 observations).

The light curve we found is very similar to those obtained by Grav, Holman & Kavelaars (2003) and Terai & Itoh (2013), both in rotation period ($11\overset{\mathrm{h}}{.}52 \pm 0\overset{\mathrm{h}}{.}14$ and $11\overset{\mathrm{h}}{.}50 \pm 0\overset{\mathrm{h}}{.}10$), and amplitude ($0\overset{\mathrm{m}}{.}029 \pm 0\overset{\mathrm{m}}{.}003$ and $0\overset{\mathrm{m}}{.}031 \pm 0\overset{\mathrm{m}}{.}001$). In Sect. 2.3 we analyse in detail the consequences of the similarities of these light curves obtained over a ∼15-year period.
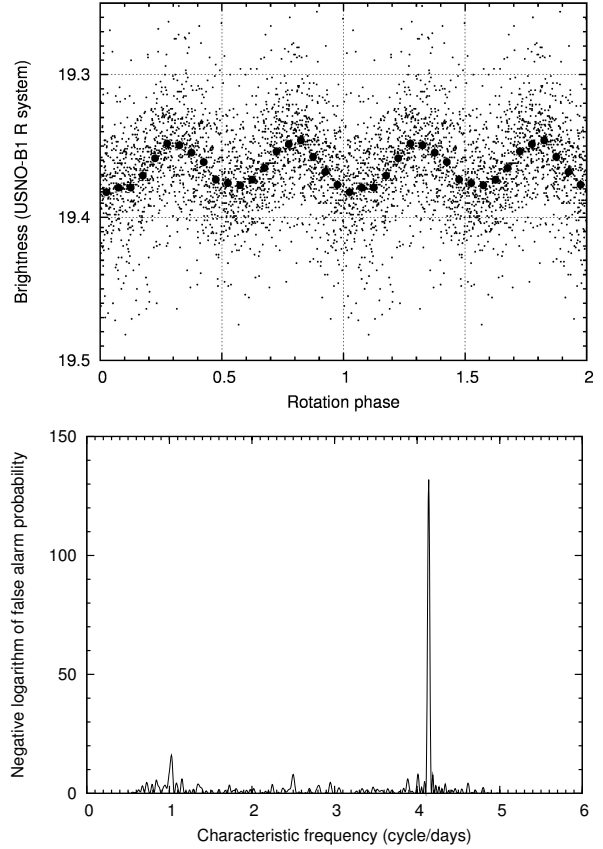
Figure 2. Upper panel: Folded and binned light curve of Nereid as reconstructed from *Kepler*/K2 data after subtracting the long-term trend caused by the increasing phase angle and distance. The binned light curve is shown above with $N = 20$ bins, the formal uncertainties of the phase-binned data poins are in the range of $0\overset{\mathrm{m}}{.}0027$–$0\overset{\mathrm{m}}{.}0033$. The light curve shown in this plot is normalized to the brightness at $T = 2,457,010$ JD, approximately at the center of the observations. The light curve is folded with a period of $P = 11.594\,\mathrm{h}$, corresponding to the double of the main frequency peak at $n = 4.140$ c/d in the lower figure panel. Lower panel: Frequency spectrum computed from the *Kepler*/K2 light curve. The prominent peak at $n = 4.140 \pm 0.006$ cycles/day can be easily recognized.

2.3   Spin axis constraints

The similarity of the 2001, 2008 and 2015 light curves puts constraints on the actual spin axis orientation. First, due to the short rotation period with respect to the orbital period (∼360 days) the precession time of the spin axis is long, at least a few hundred years, even if very elongated body and/or high original obliquity are assumed (Dobrovolskis 1995). This suggests that the spin axis of Nereid remained in approximately the same direction in the last ∼15 years. However, Neptune (and hence Nereid) moved on its orbit about 30° along the ecliptic in the last 15 years, and therefore the aspect angle ϑ of the spin axis should have changed with respect to the observer even if it was otherwise pointing in the same direction in space in this period. The position angle ϑ depends on the ecliptic coordinates of the target (λ, β) as well as on that of the spin axis' direction (λ_p, β_p):

$$\cos\vartheta = -\sin\beta\sin\beta_p - \cos\beta\cos\beta_p\cos(\lambda - \lambda_p) \quad (2)$$
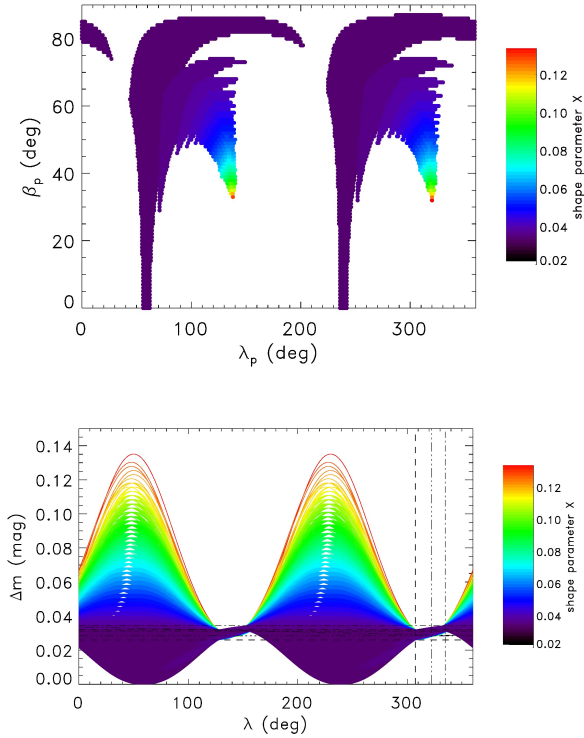
Figure 3. Possible spin axis geometry configurations that reproduce the observed light curve amplitudes in 2001, 2008 and 2015. Upper panel: Allowed ecliptic longitude and latitude of the spin axis. The colours correspond to the different X axis ratio parameters from the lowest (purple) to the highest (red, see the text for more details). Lower panel: Variation of light curve amplitude with the ecliptic longitude of Nereid assuming a stable spin axis orientation. The colours correspond to different shapes with X axis ratio parameters ranging from 0.03 to 0.14, as above. The dashed and dash-dotted *vertical* lines mark the ecliptic longitude of the 2001, 2008 and 2015 observations, respectively. The dashed and dash-dotted *horizontal* lines mark the rotation curve amplitude ranges allowed by the 2001, 2008 and 2015 observations, respectively.

If we assume that the shape of Nereid is a triaxial ellipsoid with semi-axes of $a > b > c$ then the object seen at a ϑ spin axis aspect angle will show a light curve with an amplitude of:

$$\Delta m = 2.5 log \sqrt{\frac{(b/c)^2 \cos^2 \vartheta + \sin^2 \vartheta}{(b/c)^2 \cos^2 \vartheta + (b/a)^2 \sin^2 \vartheta}} \qquad (3)$$

Here we assumed that the light curve is *solely caused by shape effects* and there are no albedo variegations on the surface. Due to the small phase angles the phase angle correction of the light curve amplitude is negligible. We characterise the semi-axis ratios of the triaxial ellipsoid by an axis ratio parameter X. With this parameter the semi-axes of the ellipsoid are:

$$b = 1, \quad a = (1 + X)b, \quad c = (1 - X)b \qquad (4)$$

and the body rotates around its shortest (c) axis.

With this assumption, and using the equations above, we calculated those $\{\lambda_p, \beta_p\}$ combinations for

which Δm corresponds to the observed light curve amplitues by Grav, Holman & Kavelaars (2003) in 2001-2002 ($\Delta m = 0.^m029 \pm 0.^m003$), Terai & Itoh (2013) in 2008 ($\Delta m = 0.^m031 \pm 0.^m001$) and by us in 2015 ($\Delta m = 0.^m0328 \pm 0.^m0018$) within the given uncertainties. In the case of the Terai & Itoh (2013) data we found the originally quoted uncertainties to be too optimistic. Our analysis of their photometry gives an amplitude uncertainty of $0.^m0026$. We used this latter value in the spin axis orientation analysis.

We originally assumed X in the $0.03 - 0.34$ range. The lowest value of X corresponds to the smallest possible X value that could produce a light curve compatible with the observations if $\vartheta = 90°$, while the highest value corresponds to a ∼2:1 *a:c* axis ratio, suggested e.g. by Hesselbrock et al. (2013). The results are plotted in Fig. 3 where the different colours mark the different axis ratio parameter values. Most of the allowed $\{\lambda_p, \beta_p\}$ pairs belong to a small X value, i.e. to a slightly elongated shape with an axis ratio of $a:c \approx 1.06:1$. The largest possible axis ratio parameter value we obtained is X = 0.133. Larger X values are not allowed by the amplitude constraints and hence more elongated shapes (X > 0.133) are excluded.

We checked how the light curve amplitude evolves in the different cases allowed by the 2001, 2008 and 2015 light curve amplitude constraints. In Fig. 3b we present the light curve amplitude variation as a function of ecliptic longitude. At the observation epochs between 2001 and 2015 (ecliptic coordinates marked by vertical lines in the figure) the light curve amplitude does not change notably and remains low, irrespective of the shape of Nereid. While there are many solutions in which the amplitude remains low (slightly non-spherical cases, purple curves) along the solar orbit of the Neptune-Nereid system, there are also cases when Nereid appears notably elongated and the light curve amplitude changes remarkably with the orbital phase around the Sun (cases marked with green to red). In these latter cases Nereid could have had its highest amplitude period in the 1960's, and still could have notably higher amplitudes in the 1980's than what we can see today. Another peak in the light curve amplitude would be expected in ∼30 years. The maximum possible light curve amplitude is $\Delta m = 0.^m13$.

For the thermal emission models that we discuss in Sects. 3.3 and 3.4 it is important to see how the spin axis aspect angles and the subsolar latitudes could change with time. We plotted the subsolar latitude β_{ss} as a function of the axis ratio parameter X in Fig. 4a for the allowed configurations at the epoch of the Spitzer/MIPS observations. The subsolar latitudes show a well defined relationship with the axis ratio parameter: at low X values β_{ss} is close to zero (equator-on configurations) then it rises quickly and reaches a maximum value of $\beta_{ss} \approx 60°$ for the largest possible values of X. While β_{ss} can change notably between the MIPS and PACS epochs (up to $\Delta\beta_{ss} \approx 15°$) for low X values, the change is rather small for higher axis ratio parameters (see Fig. 4b).
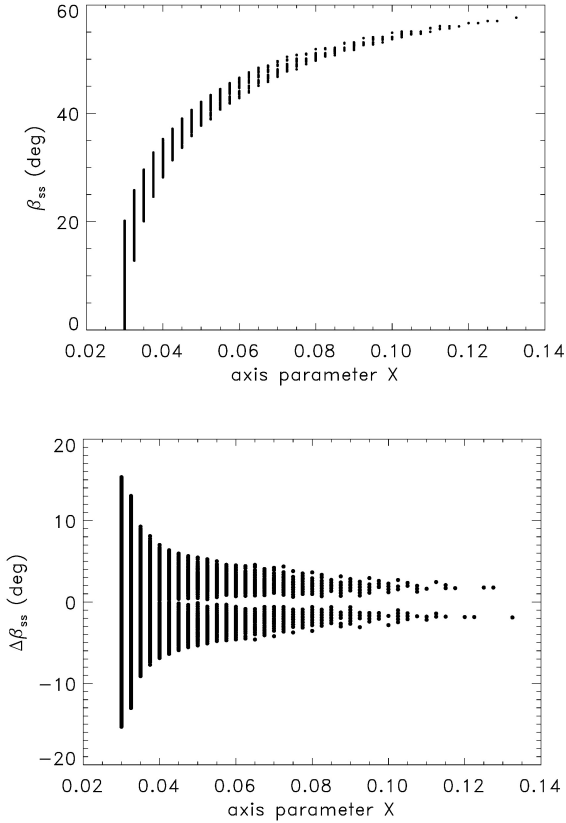
Figure 4. Upper panel: Subsolar latitude (β_{ss}) for the allowed geometry and shape configurations as a function of the axis ratio parameter X, at the Spitzer/MIPS epoch. Lower panel: Variation of the subsolar latitude between the Spitzer/MIPS and the Herschel/PACS observation epochs as a function of the axis ratio parameter X.

3 THE THERMAL EMISSION OF NEREID

3.1 Herschel Space Observatory measurements

We have found Nereid in archival Herschel Space Observations data (proposal ID: OT1_ddan01_1). The original target in these observations was Neptune, and Nereid was just accidentally on the images (see Fig. 5). Four observations were taken with the PACS (Photometer Array Camera and Spectrometer Poglitsch et al. 2010) photometer camera on board the Herschel Space Observatory (Pilbratt et al. 2010), using the 100/160 μm filter combination in all four cases. The data reduction pipeline we used is the same as the one used in the "TNOs are Cool!" Herschel Open Time Key Program (Müller et al. 2009), described in detail in Kiss et al. (2014). As our aim was to obtain photometry of a point source, we used the photProject() task with high pass filtering to create maps from the time domain detector data. The images of the four consecutive measurements were stacked in the co-moving frame of Nereid, and aperture photometry was performed on the stacked 100 and 160 μm images. Flux uncertainties were determined with the implanted source method (Kiss et al. 2014), but in this case using a $\sim$80$''$ area around Nereid rather than the high coverage regions of the whole map. As the apparent movement of the target was

very small during the measurements we were not able the perform any kind of background correction. We clearly detected Nereid in both bands, and the photometry provided $F_{100} = 22.8 \pm 1.7$ mJy and $F_{160} = 18.6 \pm 2.9$ mJy in-band flux densities at 100 and 160 μm, respectively.

3.2 Spitzer/MIPS measurements

The Spitzer Space Telescope observed Nereid in a dedicated observation in 2005 using the MIPS camera at 24 and 70 μm (Rieke et al. 2004). The data were reduced using the same pipeline as was used for the reduction of MIPS data of Centaurs and trans-Neptunian objects by Mueller et al. (2012) and Stansberry et al. (2008, 2012). Nereid was clearly detected in both bands, and we obtained in-band flux densities of $F_{24} = 2.56 \pm 0.03$ mJy at 24 μm and $F_{70} = 50 \pm 11$ mJy at 70 μm using multi-aperture photometry. The corresponding images are presented in Fig. 6. At the time of the observations Nereid was at $\sim$4$'$ separation from the very bright Neptune. While the 24 μm image (Fig. 6a) does not seem to be contaminated by extended emission features from the planet, this is not the case at 70 μm. The two bright rims at the top and bottom of the 70 μm image (Fig. 6b) are caused by the hexagon structure of the Neptunian point spread function (PSF), as it is demonstrated in Fig. 6c. There are also less apparent emission spikes at the location of Nereid that may affect the photometry. To account for the emission from Neptune at the location of Nereid, we tried to subtract Neptune's contribution by scaling a theoretical 70 μm 75 K PSF, scaled to the actual brightness of Neptune in this band at the time of the observations. Neptune's brightness was estimated using the Neptune model by R. Moreno (Moreno 2012) and we obtained $F_{70}^{Neptune} = 383.2$ Jy at the effective wavelength of 71.42 μm of this MIPS band. This model has been used for the Herschel/PACS and SPIRE flux calibration and used to reproduce the flux densities of Neptune within 2% (Müller et al., A&A, submitted). With this correction the main emission features have disappeared and repeated photometry provided an in-band flux of $F'_{70} = 29 \pm 16$ mJy.

3.3 NEATM model

We used the Near-Earth Asteroid Thermal Model (NEATM) (Harris 1998) to estimate the thermal emission of Nereid using the Spitzer/MIPS 24 and 70 μm and the Herschel/PACS 100 and 160 μm fluxes, as listed in Table 2. The Spitzer/MIPS and Herschel/PACS observations are separated by about six years, and, as we have seen above, there were indications that the rotational axis, brightness and the apparent shape of Nereid may change significantly on this timescale (see Sect. 1). However, as discussed above, the similarity of our newly detected rotation solution to those by Grav, Holman & Kavelaars (2003) and Terai & Itoh (2013) indicates that Nereid has been in a low rotational light curve amplitude period in the recent decade that is also associated with relatively small changes in spin axis rotation angle and subsolar latitude configurations. Therefore we feel that the combination of the Spitzer/MIPS and Herschel/PACS data is likely feasible and can better constrain the radiometry solutions than analysing them separately.

We characterise the radiometry solutions by calculating the reduced χ^2 values of the fits from the observed and

Table 1. Summary of Nereid's thermal infrared observations. The "identifier" column refers to OBSID in the case of PACS and AORKEY in the case of MIPS measurements.

Instrument	Obs. date (JD)	identifier	duration (s)	filter combination (μm/μm)	r_h (au)	Δ (au)	α (deg)
Herschel/PACS	2456090.655	1342222561	2996	100/160	30.02	29.65	1.85
Herschel/PACS	2456090.691	1342222562	2996	100/160			
Herschel/PACS	2456090.726	1342222563	2996	100/160			
Herschel/PACS	2456090.679	1342222564	2996	100/160			
Spitzer/MIPS	2453539.667	4535808	1012	24	30.07	29.57	1.70
Spitzer/MIPS	2453539.679	4535808	1012	70			
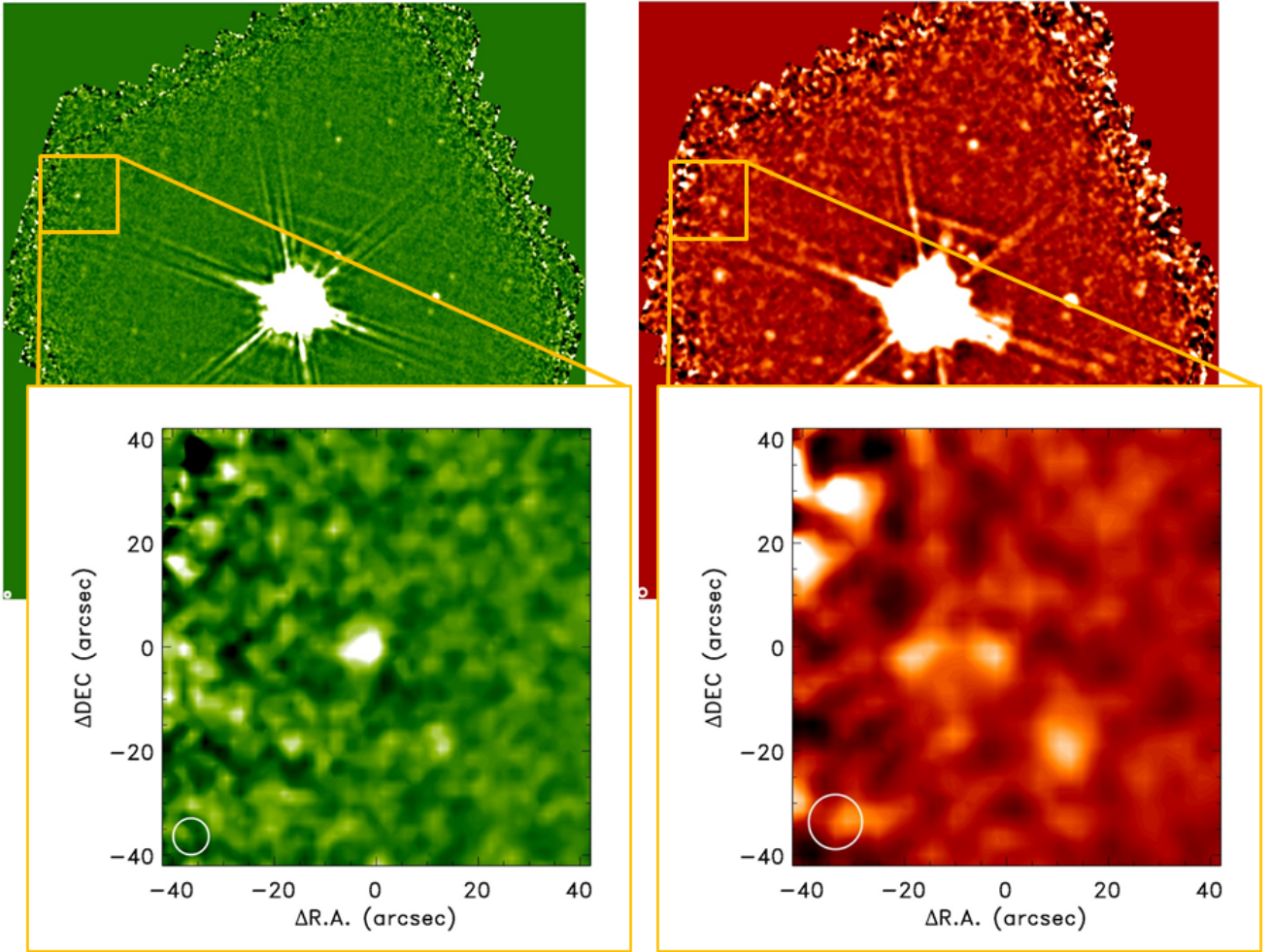
Figure 5. Nereid on the Herschel/PACS 100 μm (left) and 160 μm, co-added images, reduced in the co-moving frame of Neptune. The large images show the full area mapped with Neptune in the centre, while the zoomings show the close environment of Nereid, with the moon in the centre of the stamps. At 160 μm Nereid was identified by positional matching with other wavelengths from the multiple sources of similar brightness.

model fluxes of a specific effective diameter and beaming parameter combination. We consider a solution acceptable if $\chi^2 \leq (1+\sigma)^2$, where σ is the standard deviation of the χ^2 distribution (see e.g. Vilenius et al. 2014, for a similar application of the method). Albedo and effective diameter are not independent but are linked by the absolute magnitude. We use $H_V = 4^{\text{m}}.418 \pm 0^{\text{m}}.008$, a weighted average of the absolute

magnitudes provided by Grav, Holman & Fraser (2004) and Rabinowitz et al. (2007).

For the sake of completeness, we derived four kind of fits:

a) *MIPS 24 and 70 μm only, original 70 μm flux (MIPS epoch).* In this case we used input flux derived from the uncorrected 70 μm flux, $F_m(70) = 55.0 \pm 12.7$ mJy (see Ta-
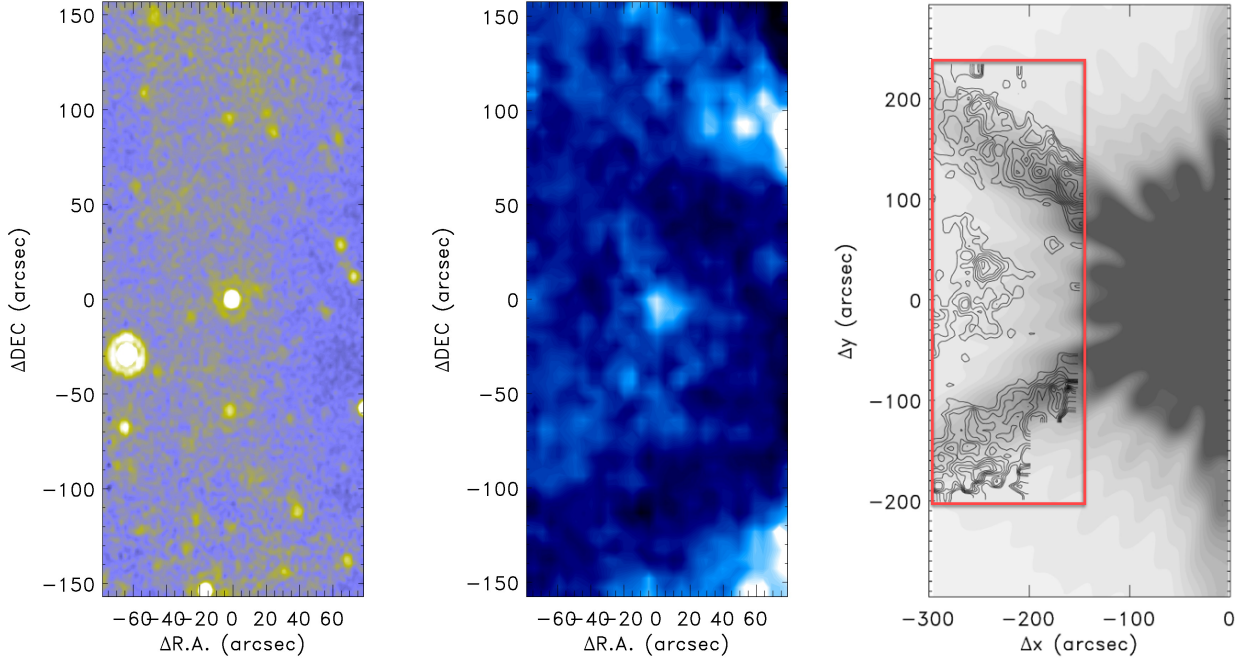
Figure 6. Nereid as observed at 24 and 70 μm with the MIPS instrument of the Spitzer Space Telescope. Left panel: 24 μm false colour image. Middle panel: 70 μm false colour image; Nereid is the bright compact source in the centre of both images. Right panel: MIPS 70 μm intensity contours (the same as the middle panel) overlaid on an intensity map (grayscale) of a model image of Neptune which was not in the field-of-view. The red rectangle shows the area of the MIPS 70 μm image. The position of the bright source relative to Nereid is set in such a way that it corresponds to the relative position of Nereid and Neptune at the time of the Spitzer/MIPS observations.

Detector/ filter	λ_{eff} (μ)m	F_i (mJy)	C_λ	F_m (mJy)
MIPS 24	23.68	2.56±0.03	0.99±0.01	2.59±0.13
MIPS 70/u	71.42	50±11	0.91±0.01	55.0±12.7
MIPS 70/c	71.42	29±16	0.91±0.01	31.9±17.6
PACS 100	100.0	22.8±1.7	0.99±0.01	23.0±2.1
PACS 160	160.0	18.6±2.9	1.03±0.01	18.1±3.0

Table 2. Spitzer/MIPS and Herschel/PACS photometry results. The columns of the table are: Detector and filter combination; F_i: inband flux, as determined from the corresponding image; λ_{eff}: effective wavelength of the band; C_λ: Colour correction factor; F_m: final, monochromatic flux, used for radiometry modelling. The F_m monochromatic fluxes are obtained as $F_m(\lambda) = F_m(\lambda)/C_\lambda$. MIPS 70/u and 70/c refer to the uncorrected and corrected 70 μm fluxes, as described in the text. An instrumental calibration accuracy of 5% was assumed for all detector/filter combinations and added quadratically to the flux uncertainties.

ble 2). The NEATM fits resulted in a best fit diameter of D = 605±95 km, η = 1.36±0.16, and p$_V$ = 0.081±0.027. (see the corresponding SED, plotted with dotted line, in Fig. 7a). This diameter is by far larger than any conceivable size for Nereid, and clearly indicates that the MIPS 70μm flux is strongly contaminated, most likely by the diffraction spikes of Neptune, as discussed in Sect. 3.2 earlier. Therefore this 70 μm input flux and the related solution is not considered any further in our analysis.

b) *MIPS 24 and 70 μm only, corrected 70 μm flux (MIPS epoch)*. In Fig. 7b we plot the regions of the acceptable solution ($\chi^2 \leq (1+\sigma)^2$) in the diameter – beaming parameter space. For Case *b* this is represented by the area enclosed by dashed lines. Due to the large error bar of the 70 μm flux a wide range of diameters, and an especially wide range of beaming parameters are allowed.

c) *PACS 100 and 160 μm only (PACS epoch)*. When only the PACS measurements are considered the situation is somewhat different. Here we have a strong correlation of the diameter and η, but the model is not well constrained due to the lack of short wavelength fluxes (region enclosed by dash-dotted lines in Fig. 7**b**).

d) *PACS and MIPS combined (corrected 70 μm flux, both MIPS and PACS epochs)*. Due to the similarities of the observing geometries at the dates of the MIPS and PACS observations the resulting fluxes of the same NEATM model are almost equivalent for the two epochs, and therefore a mean observing geometry can be safely applied on the combined dataset (see Table 1). When all four data points are considered, the NEATM model becomes well constrained. The common solution (gray contour ellipses in Fig. 7b) is compatible with both the MIPS-only and the PACS-only solutions (Cases *b* and *c*). In this case we obtain D = 345±15 km, η = 0.76±0.02, and p$_V$ = 0.25±0.02. This effective diameter is very similar to the Voyager-2 flyby value of 350±50 km (Thomas et al. 1991). The low χ^2 value obtained for this combined solution confirms that the η values related to the two epochs are the same to a level that they cannot be distinguished with the current flux uncertainties.

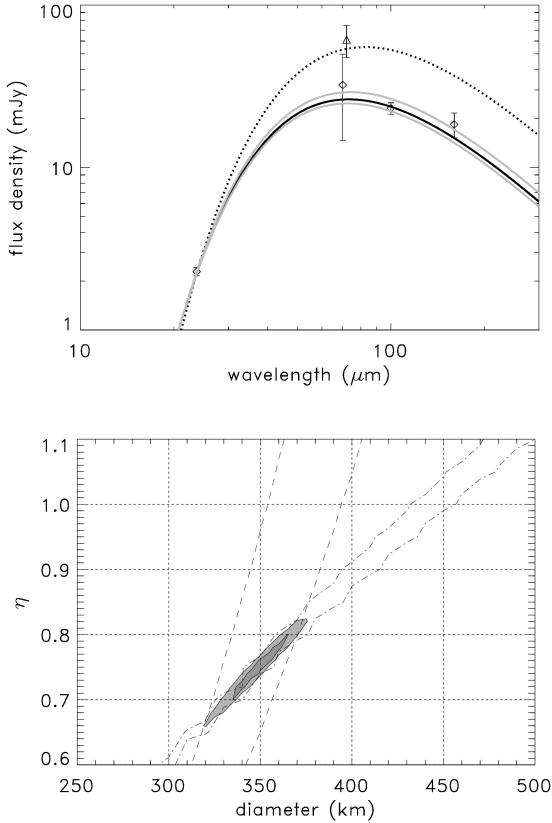We consider the combined dataset and the solution of

Figure 7. Upper panel: Best-fit NEATM model of the thermal emission of Nereid with the observed and colour corrected fluxes overplotted (Case d, diamond symbols and solid line). The $\chi^2 = (1+\sigma)^2$ NEATM fits are drawn by gray curves. The NEATM fit using the uncorrected MIPS 70 μm flux, corresponding to Case a, is also plotted with a dotted curve. The uncorrected 70 μm plot is presented by a triangle and slightly shifted in wavelength from the uncorrected point for clarity. Lower panel: Reduced χ^2 contour map of the NEATM model fits as a function of the effective diameter and the beaming parameter η. The outermost contour of 1.7 correspond to the reduced χ^2 limit of acceptable models with four data points and two model parameters (diameter and η)

Case d as the most acceptable size, albedo and beaming parameter for Nereid. It is supported by the light curve analysis / spin axis constraints and none of the other NEATM solutions (Cases b and c) contradict with solution d considering all the errors in the NEATM model parameter determination.

Using our favoured radiometry solution of $D = 345 \pm 15$ km, $\eta = 0.76 \pm 0.02$, and following the relations of thermal parameter, beaming parameter and surface roughness described in Spencer et al. (1989) and Spencer (1990), we can constrain the thermal properties (thermal inertia and surface roughness) of Nereid using the NEATM solutions to some level. In the framework of the above-mentioned models, a beaming parameter below unity can be explained by surface roughness effects. The minimum level of surface roughness beaming contribution required to obtain $\eta = 0.76$ (our best-fit value) is $\delta\eta = 0.24$ (see eq. 7 in Spencer 1990) that corresponds to an r.m.s. surface

roughness level of $\rho = 0.6$ (Lagerros 1998). Such a surface can also be constructed by considering 90° hemispheral craters with 50 per cent surface coverage. To obtain this low η, it is, however, required in addition to the moderately high surface roughness that either the thermal inertia is extremely low $(\Gamma < 0.1\,J\,m^{-2}\,s^{-1/2}\,K^{-1})$ *or* the subsolar latitude is $\beta_{ss} \approx 90°$ (we see the spin-axis near to pole-on). For a near to pole-on configuration the thermal intertia should still be low, but it can be a value somewhat higher than in general case, typically $\Gamma \approx 2\,J\,m^{-2}\,s^{-1/2}\,K^{-1}$ may be possible. The other possibility, $\beta_{ss} \approx 90°$ is not supported by the light curve constraints, as a maximum value of $\beta_{ss} \approx 60°$ is obtained in the spin axis analysis (see Sect. 2.3 and Fig. 4).

If we allow for a high surface roughness $(\rho = 0.9$ that can be achieved with 90° craters at 100% coverage), different sub-solar latitudes become possible. E.g. for $\beta_{ss} = 0°$ $\eta = 0.76$ results in a very low thermal inertia of $\Gamma = 0.5\,J\,m^{-2}\,s^{-1/2}\,K^{-1}$. Lellouch et al. (2013) found an average thermal inertia of $\Gamma = 2.5 \pm 0.5\,J\,m^{-2}\,s^{-1/2}\,K^{-1}$ among Centaurs and trans-Neptunian objects in the heliocentric distance range of $25\,au < r_h < 41\,au$, with a strong suggestion of decreasing Γ with increasing heliocentric distance. Even higher values of Γ are expected among the icy moons of the outer giant planets. This may indicate that the observed values of the beaming parameter may rather be explained by a higher subsolar latitude $(\beta_{ss} \approx 60°)$ than by a very low thermal inertia value of the surface. This also suggests that the shape of Nereid may be elongated to some level, because high β_{ss} values are found for larger axis ratio parameters in Sect. 2.3.

3.4 Thermophysical modelling

We also used a thermophysical model (TPM, see Lagerros 1996, 1997, 1998; Müller & Lagerros 1998, 2002). to characterise the thermal emission of Nereid. The TPM calculates the temperature distribution on the surface of a body for a specific shape, illumination, observing geometry, spin axis direction and rotation period. The model considers the thermal properties of the surface directly, including thermal inertia and surface roughness.

We looked for solutions that matches the observed Spitzer/MIPS and Herschel/PACS far infrared fluxes the best, using the input fluxes listed in Table 2. As in the case of the NEATM model, we characterise the goodness of fit by calculating the reduced χ^2 values and we require that acceptable solutions should fulfil the requirement of $\chi_r^2 \leq (1+\sigma)^2$.

Low $(\rho = 0.1)$ to intermediate $(\rho = 0.5)$ surface roughness cannot explain the observed fluxes as these values result in very high $(\chi_r^2 \gg 3)$ reduced χ^2. All acceptable solutions $(\chi_r^2 < 1.7)$ are related to "hot model settings", i.e., very high roughness $(\rho \geq 0.7)$ combined with extremely low thermal inertia $(\Gamma \ll 1\,J\,m^{-2}\,s^{-1/2}\,K^{-1})$, except for configurations near to pole-on where hot temperatures are reached for a wider range of thermal inertias, as in these cases heat is not transported to the night side. All acceptable settings $(\chi_r^2 < 1.7)$ produce size and albedo solutions with $D_{eff} = 353$–362 km and $p_V = 0.23$–0.25.

Assuming that Nereid has a thermal inertia in the range of 1–$5\,J\,m^{-2}\,s^{-1/2}\,K^{-1}$, comparable to typical TNOs/Centaurs at similar distances (see Lellouch et al.
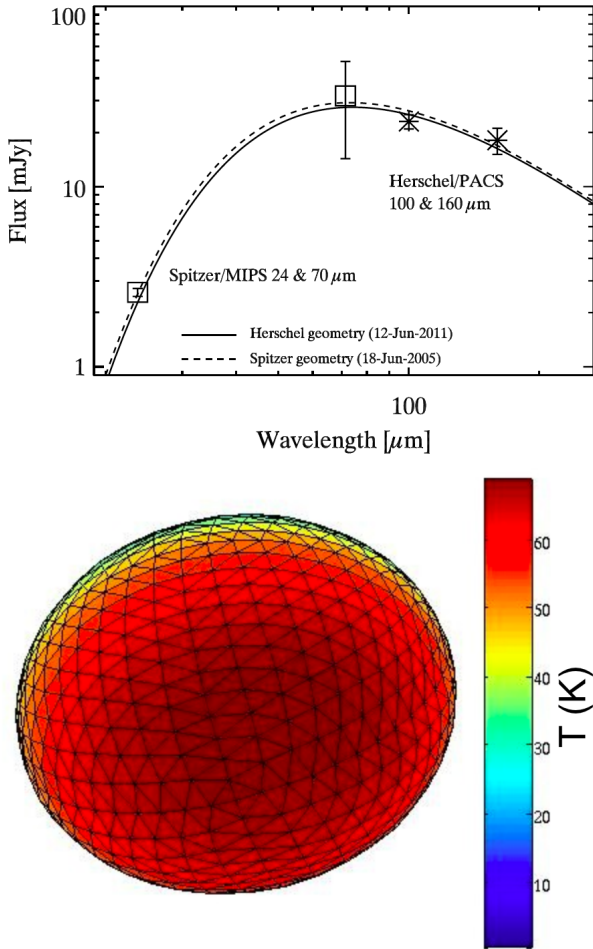
Figure 8. Upper panel: Best fit TPM model of the thermal emission of Nereid for an axis ratio parameter of $X = 0.0133$ and a spin axis orientation of $\lambda_p = 320°$ and $\beta_p = 32°$. The solid and dashed lines correspond to the observing geometries at the Herschel/PACS and Spitzer/MIPS observation epochs, respectively. Lower panel: Temperature distribution of the model above.

2013), only model settings with a spin axis direction close to "pole-on", $\{\lambda_p, \beta_p\} = \{320\pm30°, 0\pm30°\}$, produce acceptable flux predictions. The best-fit case of these models provided an effective size of $D = 357\pm13$ km and a geometric albedo of $p_V = 0.24\pm0.02$.

Our TPM analysis above suggested a high subsolar latitude and a correspondingly low spin axis aspect angle. According to the spin-axis constraints discussed in Sect. 2.3 high β_{ss} may occur for the highest possible axis ratio parameters only. This favours shape solutions of $X \approx 0.13$, and a corresponding subsolar latitude of $\beta_{ss} \approx 60°$ (see Fig. 4). We have chosen the highest possible shape parameter value of $X = 0.133$ (a:c = 1.3:1) and the corresponding subsolar latitude of $\beta_{ss} = 58°$, and tested the feasibility of this configuration in a TPM model. When high roughness ($\rho = 0.9$) is assumed we obtained an acceptable χ_r^2 value of 1.2, but this is associated with a very low thermal inertia of $\Gamma = 0.5\ J\ m^{-2}\ s^{-1/2}\ K^{-1}$. For this solution the best fit effective diameter is $D = 335$ km, with a correspondig geometric albedo of $p_V = 0.275$. Application of an extreme roughness of $\rho = 1.0$ provides very low reduced χ^2 values of ~0.5,

even when the "nominal" $\Gamma = 5\ J\ m^{-2}\ s^{-1/2}\ K^{-1}$ thermal inertia values are used. However, in these cases we obtain a somewhat smaller size of $D = 326$ km and a higher albedo of $p_V = 0.29$.

4 DISCUSSION

The most important question about Nereid, as discussed in the literature, was its shape and the precession behaviour of its spin axis. This was modelled in detail by Schaefer et al. (2008) and Hesselbrock et al. (2013), with the main aim to explain the large amplitude brightness variations seen on different time scales. These models assumed a long rotation period (72–144 h) which was needed to achieve precession timescales of around a decade.

One important finding of our paper is that we confirmed the short ($11^h.594$) rotation period observed earlier by Grav, Holman & Kavelaars (2003) and Terai & Itoh (2013). As it has been mentioned previously, a short rotation period implies a long spin axis precession time, as $P_{prec} \propto P_{orb}^2 / P_{spin}$, where P_{prec} is the precession period, P_{orb} is the orbital period around Neptune, and P_{spin} is the rotation period (see e.g. Hesselbrock et al. 2013). P_{prec} values calculated from the $11^h.594$ rotation period are at least an order of magnitude longer than those assumed by Schaefer et al. (2008) and Hesselbrock et al. (2013), even if an extremely elongated body is assumed. Therefore the spin axis orientation could not change significantly in the last ~15 years, and the precession of the spin axis cannot be the reason behind the large flux variations observed.

In Sect. 2.3 we used this stability of the spin axis orientation and obtained a maximum axis ratio of a:c = 1.3 from the light curve amplitude analysis. According to Hesselbrock et al. (2013), forced precession of Nereid could be feasible only if the moon is considerably elongated with an *a:c* axis ratio of $\sim1.9:1$. Such a high axis ratio is excluded by our results, consistently with the long precession timescales obtained.

The shape solution favoured by the thermal analysis (axis ratio parameter of $X = 0.133$) is also the one that provides the maximum possible light curve amplitude of $\Delta m \approx 0^m.13$, with a peak in the 1960's (see Sect. 2.3). Even this solution is unable to explain the extremely large brightness variations observed some decades ago (up to Δm of $0^m.5$, see fig. 4 in Schaefer et al. 2008, for a summary of these data). Whatever caused these variations, it cannot be the forced precession of a very elongated Nereid, as this scenario is inconsistent with our present data.

The long rotation period assumed by Schaefer et al. (2008) and Hesselbrock et al. (2013) was partly based on the expectation that if Nereid was formed around Neptune or captured at early times, then its original rotation – which could have had a period of a few hours – should have slowed down considerably, even if Nereid is just slightly elongated. In this sense, Nereid rotates fast today – this may favour a late capture (i.e. Nereid did not have enough time to slow down considerably) or indicate some other influence, like a collision, that may overwrite the rotational state. We note that Grav, Holman & Fraser (2004) suggested that Halimede, a small moon of Neptune, may be a fragment of Nereid broken off during a collision. This scenario for the

origin of Halimede is supported by their similar colours and the relatively high probability of a collision between Nereid and Halimede in the timespan between the formation of the Solar System and today (Holman et al. 2004).

As discussed in detail in Schaefer et al. (2008), the Voyager-2 images analysed by Thomas et al. (1991) could hardly be used to put constraints on the actual shape of Nereid, i.e. we did not have enough information to tell whether Nereid was spherical or notably non-spherical. The combination of the spin axis constrains and both the NEATM and TPM radiometry results favors a moderately elongated shape with a axis ratio parameter $X \approx 0.13$, and correspondingly a present subsolar latitude of $\beta_{ss} \approx 60°$ (a possible shape solution using $X = 0.133$ is presented in Fig. 8b). The moderately elongated shape put forward here for Nereid is feasible regarding observational constraints. However, for a moon of $\sim$350 km in diameter a shape closer to spherical may be more likely (see e.g. Schaefer et al. 2008) based on the shape information of giant planet moons of similar size. Most of these large ($>$100 km in radius) moons are round to a few per cent (better than 10%) accuracy. Our preferred solution for Nereid is further away from a perfect sphere. One exception among these satellites may be the Saturn moon, Hyperion, which is highly elongated despite that it is similar in size to Nereid (about 205×130×110 km semi-axes). In the case of Hyperion the elongated shape is explained by the high porosity of the interior ($\sim$40%) that also leads to a 'sponge-like', high roughness surface where craters remain nearly unchanged over billions of years (Thomas et al. 2007). A porous internal structure and high roughness surface similar to that of Hyperion may explain well both the elongated shape and the radiometry analysis results obtained for Nereid in the present paper.

In a recent paper Lacerda et al. (2014) presented an analysis of colours and albedos of Centaurs and trans-Neptunian objects, and identified two main groups whose existence can be considered as an evidence for a compositional discontinuity in the young Solar System. For comparison, we plotted the colour and albedo of Nereid in a diagram (Fig. 9) similar to fig. 2 in Lacerda et al. (2014), presenting these dark-neutral and bright-red objects. Colours are represented by spectral slopes, calculated in the same way as in Lacerda et al. (2014). If Nereid was either formed around Neptune or captured during Neptun's outward migration from the 20-30 au distance range in the early Solar System, it is expected to exhibit a surface similar to the objects in the dark-neutral group. Indeed, Nereid is close in colour to the typical colours of objects in this group, but at the same time, its albedo is significantly larger than the typical value in this group, even larger than the albedos of most objects in the bright-red group. If Nereid was a member to the dark-neutral group, it would have the brightest surface among these objects. While Nereid is at the edge of the distributions of objects of both major groups in the albedo-colour plain, it is rather close in these characteristics to the Saturnian moon Hyperion (purple triangle in Fig. 9). As mentioned earlier, the surface roughness and internal structure of Nereid may as well be similar to those characteristic of this irregular satellite.
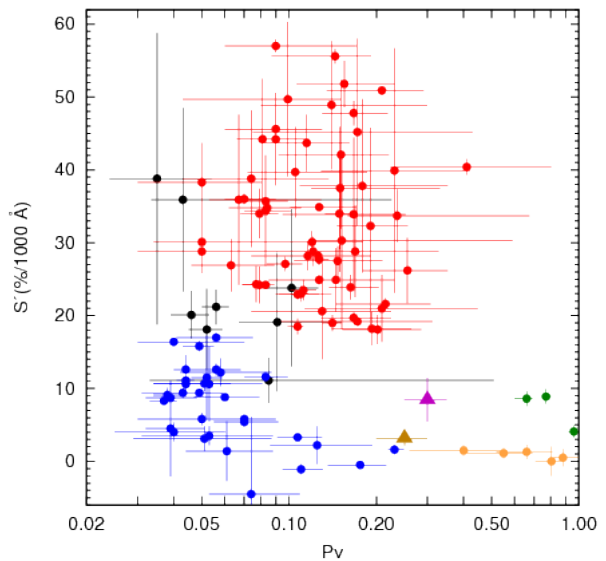

Figure 9. Albedo-colour diagram of Centaurs and trans-Neptunian objects, also presenting the colours and albedos of Nereid (brown triangle, data from this paper and Grav, Holman & Fraser 2004) and Hyperion (purple triangle, Hicks et al. 2008; Thomas 2010). The colours and albedos of the other objects are taken from the original resources cited in Lacerda et al. (2014). The colours of the symbols are the same as in Lacerda et al. (2014): red dots – bright-red group, blue dots – dark-neutral group, orange dots – Haumea-type objects, green-dots – largest TNOs, **black-dots – objects with large uncertainties and ambiguous surface type**.

5   SUMMARY

In this paper we presented space born observation of Nereid, performed by the Kepler Space Telescope in the framework of the extended K2 mission, and results obtained from archival infrared data of the Spitzer Space Telescope and the Herschel Space Observatory. From the Kepler K2 data we obtained a light curve that was the same in period and similar in amplitude to those obtained from ground based observations in 2001 and 2008. These observations together contrain the possible rotation states of Nereid very well. According to these results, Nereid is in a low amplitude apparent light curve state nowadays, but may have been in a much larger amplitude state some decades ago. We managed to exclude very elongated shapes with axis ratios above 1.3:1; this also means that Nereid cannot be in a forced precession state due to tidal forces as it is not elongated enough for this process. This is a robust result as we assumed that the light curve of Nereid is solely caused by shape effects and albedo variegations existing on the surfce would just make the moon more spherical in this respect.

We confirmed the size of Nereid obtained from Voyager-2 flyby data by an independent method – radiometry based on infrared data. Both the NEATM and TPM thermal emission models resulted in similar effective size (D =335–345 km) and albedo values ($p_V = 0.25$–0.27). Both methods indicate very high roughness (likely $\rho \approx 0.9$) independently of shape, i.e. a surface with deep craters and very high surface coverage. Using the light curve and thermal emission results together we obtain a likely moderately elongated shape

(a:c ≈ 1.3:1) and a present spin axis aspect angle of $\vartheta \approx 30°$ for this irregular moon of Neptune. This shape may partly explain the larger light curves amplitudes observed some decades ago.

ACKNOWLEDGEMENTS

REFERENCES

Dobrovolskis, A.R., 1995, Icarus, 118, 181
Gilliland, R. L. et al., 2010, ApJL, 713, 160
Grav, T.; Holman, M. J. & Kavelaars, J. J., 2003, ApJ, 591, L71
Grav, T.; Holman, M. J. & Fraser, W.C., 2004, ApJ, 613, L77
Harris, A. W., 1998 Icarus, 131, 291
Hesselbrock, A.J., Alexander, S.G., Thomas, W.H., Abel, N.P., 2013, AJ, 145, 144
Hicks, M.D., Buratti, B,J., Basilier, E.N., 2008, Icarus, 193, 352
Holman, M.J., Kavelaars, J.J., Grav, T., et al., 2004, Nature, 430, 865
Howell, S. B., Sobeck, C., Haas, M., et al. 2014, PASP, 126, 398
Jacobson, R. A. 2009, AJ, 137, 4322
Kiss, Cs., Müller, T. G., Vilenius, E., et al., 2014, Experimental Astronomy, 37, 161
Lacerda, P., Fornasier, S., Lellouch, E., et al. 2014, ApJL, 793, 2
Lagerros, J. S. V., 1996, A&A, 310, 1011
Lagerros, J. S. V., 1997, A&A, 325, 1226
Lagerros, J. S. V., 1998, A&A, 332, 1123
Lellouch, E., Santos-Sanz, P., Lacerda, P., et al., 2013, A&A, 557, A60
Monet, D. G., Levine, S. E.; Canzian, B., et al. 2003, AJ, 125, 984
Moreno, R. (2012), Neptune and Uranus planetary brightness temperature tabulation. Tech. rep., ESA Herschel Science Centre, available from ftp://ftp.sciops.esa.int/pub/hsc-calibration/PlanetaryModels/ESA4/
Müller, T. G. & Lagerros, J. S. V. 1998, A&A, 338, 340

Müller, T.G., Lellouch, E., Böhnhardt, H., et al., 2009, EM&P, 105, 209
Müller, T. G. & Lagerros, J. S. V. 2002, A&A, 381, 324
Müller, T. G., Lellouch, E, Böhnhardt, H. et al. 2009, EM&P, 105, 209
Mueller, M., Stansberry, J., Mommert, M. & Grundy, W., 2012, "TNO Diameters And Albedos: The Final MIPS Dataset", AAS DPS meeting, #44, #310.13
Pál, A., 2012, MNRAS, 421, 1825
Pál, A.; Szabó, R.; Szabó, Gy. M.; Kiss, L. L.; Molnár, L.; Sárneczky, K. & Kiss, Cs. 2015a, ApJL, 804, 45
Pál, A.; Kiss, Cs.; Müller, Th. G.; Molnár, L.; Szabó, R.; Szabó, Gy. M.; Sárneczky, K.; Kiss, L. L. 2015c, AJ, submitted
Pilbratt, G. L., Riedinger, J. R., Passvogel, T., et al., 2010, A&A, 518, L1
Poglitsch, A., Waelkens, C., Geis, N., et al., 2010, A&A, 518, L2
Rabinowitz, D., Schaefer, B.E., & Tourtellotte, S.W., 2007, AJ, 133, 26
Rieke, G.H., Young, E.T., Engelbracht, C.W., et al., 2004, ApJS, 154, 25
Schaefer, B.E., Tourtellotte, S.W., Rabinowitz, D.L., Schaefer, M.W., 2008, Icarus, 196, 225
Stansberry, J., Grundy, W.M., Brown, M.E., et al., 2008, in The Solar System Beyond Neptune, Physical Properties of Kuiper Belt and Centaur Objects: Constraints from the Spitzer Space Telescope, p.161 (Tuscon, AZ: Univ. Arizona Press)
Stansberry, J.A., Grundy, W.M., Mueller, M., et al., 2012, Icarus, 219, 676
Szabó, R., Sárneczky, K., Szabó, Gy. M., et al. 2015, AJ, 149, 112
Terai, T. & Itoh, Y., 2013, PASJ, 65, 46
Thomas, P., Veverka, J., Helfenstein, P., 1991, J. Geophys. Res., 96, 19253
Thomas, P.C., Armstrong, J.W., Asmar, S.W., et al., 2007, Nature, 448, 50
Thomas, P.C., 2010, Icarus, 208, 395
Vilenius, E., Kiss, C., Müller, T. et al. 2014, A&A, 564, 35